nature communications

Article

https://doi.org/10.1038/s41467-024-55098-w

Development of patient-derived lymphomoids with preserved tumor architecture for lymphoma therapy screening

Received: 5 June 2024

Accepted: 2 December 2024

Albert Santamaria-Martínez [1,2], **Justine Epiney** [1,2,3], **Divyanshu Srivastava** [1,2,4,5], **Daniele Tavernari** [1,2,4,5], **Marco Varrone** [2,4,5], **Dina Milowich** [6], **Igor Letovanec** [6], **Thorsten Krueger** [7], **Rafael Duran** [8], **Giovanni Ciriello** [2,4,5], **Anne Cairoli** [3] & **Elisa Oricchio** [1,2]

The efficacy of anti-cancer therapies depends on the genomic composition of the tumor, its microenvironment, spatial organization, and intra-tumor heterogeneity. B-cell lymphomas are a heterogeneous group of tumors emerging from B-cells at different stages of differentiation and exhibiting tumor-specific interactions with the tumor microenvironment. Thus, the effect of drug treatments can be influenced by the tumor composition and functional interactions among immune cells. Here, we develop a platform to maintain small fragments of human lymphoma tissue in culture for several days, and use them to test response to small molecules. We collect 27 patient samples representative of different lymphoma subtypes, and establish ex vivo tissue fragments that retain histological, cellular, and molecular characteristics of the original tissue, here referred to as lymphomoids. Using lymphomoids, we test sensitivity to several clinically approved drugs in parallel and examine tissue remodeling upon treatment. Moreover, when this information is available, we show that the effect of the inhibitors observed in lymphomoids is consistent with the patients' response in the clinic. Thus, lymphomoids represent an innovative ex vivo model to assess the effect of anti-cancer therapies while preserving the tissue structure and its components.

Each tumor is characterized by a unique combination of molecular alterations and transformed cells establish a myriad of interactions with immune and stromal cells[1]. Tumor heterogeneity and plasticity hinder the selection of appropriate therapies for each cancer patient. To address this problem, experimental models based on patients' biopsies have started to emerge and they are typically referred to as tumor avatars[2]. These models are used to assess sensitivity to different therapies directly on tumor tissues derived from each patient to guide

---

[1]Swiss Institute for Experimental Cancer Research, École Polytechnique Fédérale de Lausanne (EPFL), Lausanne, Switzerland. [2]Swiss Cancer Center Léman, Lausanne, Switzerland. [3]Division of Hematology and Central Hematology Laboratory, Centre Hospitalier Universitaire Vaudois (CHUV), Lausanne, Switzerland. [4]Department of Computational Biology, University of Lausanne, Lausanne, Switzerland. [5]Swiss Institute of Bioinformatics (SIB), Lausanne, Switzerland. [6]Institut Central des Hôpitaux (ICH), Hôpital du Valais, Sion, Switzerland. [7]Thoracic Surgery Department, CHUV, Lausanne, Switzerland. [8]Department of Diagnostic and Interventional Radiology, Centre Hospitalier Universitaire Vaudois (CHUV), Lausanne, Switzerland. e-mail: albert.santamariamartinez@epfl.ch; elisa.oricchio@epfl.ch

the selection of personalized treatments. In this context, patient-derived xenograft (PDX) models have been established in both solid tumors and hematological malignancies[3]. However, PDX models are time-consuming, lack the tumor microenvironment, and are more suitable to study aggressive tumors. As alternatives, the development of ex vivo models such as organoids and patient-derived tissue explants has allowed testing response to therapies in some solid tumors[4–11], but there is a scarcity of such models in B-cell lymphomas. In particular, 3D models of B-cell lymphomas are currently based on aggregates or spheroids of available cell lines or primary patient samples[12–19], but they don't retain the complex architecture of lymphoid tissue.

Non-Hodgkin lymphoma (NHL) is a diverse group of tumors originating from mature lymphocytes blocked at various stages of differentiation that accumulate heterogeneous genetic and epigenetic modifications[20–29]. NHL subtypes can be divided into indolent and aggressive tumors, where follicular lymphoma (FL) represents the most common subtype of indolent NHL, and diffuse large B cell lymphoma (DLBCL) the most common subtype of aggressive NHL[30–34]. Further subclassifications are based on the cell of origin[33], molecular profile[35,36], and their localization in distinct and specialized areas of the lymph nodes[37]. For example, FL, DLBCL, and Burkitt lymphoma (BL) originate from B-cells in germinal centers, while mantle cell lymphoma (MCL) or marginal zone B-cell lymphoma (MZL) arise from B-cells in the mantle and marginal zones, respectively. In addition, the tumor architecture as well as the extent and type of interactions between lymphoma cells and the tumor microenvironment are variable among different tumor subtypes[38–40]. For instance, follicular lymphoma retains a follicular pattern, reminiscent of the lymph node's architecture and cellularity; in contrast, DLBCL commonly exhibits architectural effacement[33]. Despite this heterogeneity, the first-line therapy is similar for most patients diagnosed with B-cell lymphomas and it includes a combination of immunochemotherapy, where R-CHOP (Rituximab, cyclophosphamide, hydroxydaunorubicin, oncovin, prednisolone) is the most common regimen[41]. Between 60 and 70% of newly diagnosed B-cell lymphomas are cured with R-CHOP treatment; however, patients with relapsed or refractory (R/R) disease have restricted therapeutic alternatives and their prognosis is limited, with low curative perspectives. The subsequent lines of treatments include T-cell-engaging therapies such as CAR-T cells and also small molecules blocking key oncogenic signaling pathways which have been approved for the treatment of aggressive lymphoma, FL, and MCL[42–45]. For instance, Bruton's Tyrosine Kinase (BTK) inhibitors such as ibrutinib or acalabrutinib can be used for the treatment of SLL, MZL, and MCL, while lenalidomide has been approved for R/R FL, MZL, and MCL in combination with rituximab. However, the number of patients that will exhibit prolonged event-free survival remains low, possibly due to the remarkable heterogeneity of the disease.

In this work, we develop a strategy to culture ex vivo lymphoma tissue fragments retaining the architecture and cellular composition of the original tissue. We use this system to test the effect of a panel of targeted therapies and immunomodulatory agents on multiple human biopsies. We observe selective sensitivity to the therapies after a few days of treatment, and in few cases where the ex vivo treatment matches the treatment of the patient in the clinic, drug sensitivity is consistent with the clinical response.

Results

Development of a system to maintain lymphoma explants in culture

B-cell lymphoma arises in lymphoid organs which are composed of multiple immune cells that are organized in specialized areas. Thus, we wanted to develop a system that preserves the viability, proliferation, structure, and cellular composition of lymphoma tissues ex vivo. To this purpose, we adapted the air–liquid interface (ALI) method[46] and we used this system to determine therapy efficacy in human lymphoma samples (Fig. 1a). Initially, we optimized the conditions to maintain lymphoma explants in culture for several weeks by using secondary lymphoid organs isolated from vavP-Bcl2 transgenic mice. These animals develop tumors that recapitulate essential aspects of human FL[47]. We produced tissue fragments between 0.75 and 1.5 mm^3 from the spleens of aged vavP-Bcl2 mice that had developed FL. Tissue fragments were embedded in an RGD-hydrogel (arginyl-glycyl-aspartic acid hydrogel), which was diluted with different amounts of growth media to modulate the hydrogel stiffness (Supplementary Fig. 1a, b). To sustain B-cell viability, we added B-cell activating factor (BAFF) (Supplementary Fig. 1c) and we tested it in combination with different cocktails of cytokines, chemokines, and small molecules. Flow cytometry analyses revealed that, except for BAFF, none of the additional molecules significantly improved viability, while IL2 significantly reduced the total number of B-cell and germinal-center B-cells after 2 weeks in culture (Supplementary Figs. 1d, 2, and Supplementary Table 1). Thus, we selected as optimal growth conditions intermediate hydrogel stiffness (1 part gel: 1 part growth medium, ~490 G'Pa) plus BAFF to guarantee good physical support to the tissue fragments while maintaining cell viability between 70 and 80% in the first week (Supplementary Fig. 1b–d). Using these conditions, tumor fragments after 1 week largely retained the tissue architecture of the spleen with recognizable enlarged follicular structures (Fig. 1b). Hence, we named these lymphoma explants lymphomoids. Next, we combined imaging and flow cytometry analyses to assess the tissue architecture and cellular organization of lymphomoids maintained in culture for 4 to 5 weeks (Fig. 1c–f). By multicolor immunofluorescence staining, we were able to distinguish four main cell populations: B-cells (B220), CD8+ T-cells, CD4+ T-cells, and macrophages (F4/80). After digitalization and quantification of the fluorescence signal intensity in multiple independent lymphomoids, we observed that the number of B-cells was preserved ex vivo, although after 3 weeks CD4+ T-cells tended to increase, while CD8+ T-cells and macrophages gradually decreased (Fig. 1c, d). Interestingly, the percentage of proliferating B-cells was similar between lymphomoids and the original spleen from which the lymphomoids were generated, and it was maintained over time (Fig. 1e). These results indicated that the cellular and structural composition of the original tissue was preserved for 1 to 2 weeks, and the proliferative capacity of the B-cells for 5 weeks. Then, we used flow cytometry analyses to characterize B and T-cell subpopulations. We quantified cell viability, the number of B-cells (B220+), germinal center B-cells (CD95+/GL7+), CD3+, CD8+, and CD4+ T-cells, and CD4+ T-follicular helper cells (Tfh) for 4 weeks, and we used the original spleen from which the lymphomoids were generated as reference. First, we observed a reduction of 20–30% in overall cell viability in the first week in culture, which concerned primarily peripheral cells in the first 48 h of the culture (Fig. 1f and Supplementary Fig. 1e, f). The number of B-cells was maintained with a modest decrease after 3 weeks, similar to what was detected in the imaging analyses. This could be associated with a gradual loss of double-positive CD95 +/GL7 + GC B-cells (Fig. 1f), although we noticed a tendency for B-cells to lose CD95 expression, but not GL7 (Supplementary Fig. 1g). In addition, the percentage of CD3+, CD8+, and CD4+ T-cells was constant, while CD4+ Tfh increased (Fig. 1f). Hence, flow cytometry and imaging analyses were overall consistent. Lastly, to determine if the cells in the lymphomoids also retained the transcriptional profile of the cells in the original tissue, we analyzed six lymphomoids derived from the spleens of two animals, after 1 or 2 weeks in culture, and the original spleen tissues by single-cell RNA-sequencing. Cells clustered independently of the tissue of origin in two major groups: T-cells identified by CD3 expression and B-cells as CD79a positive (Fig. 1g, h). Unbiased cluster analyses revealed the presence of two B-cell subpopulations (cluster 1 and cluster 3), but not in T-cells (cluster 2)

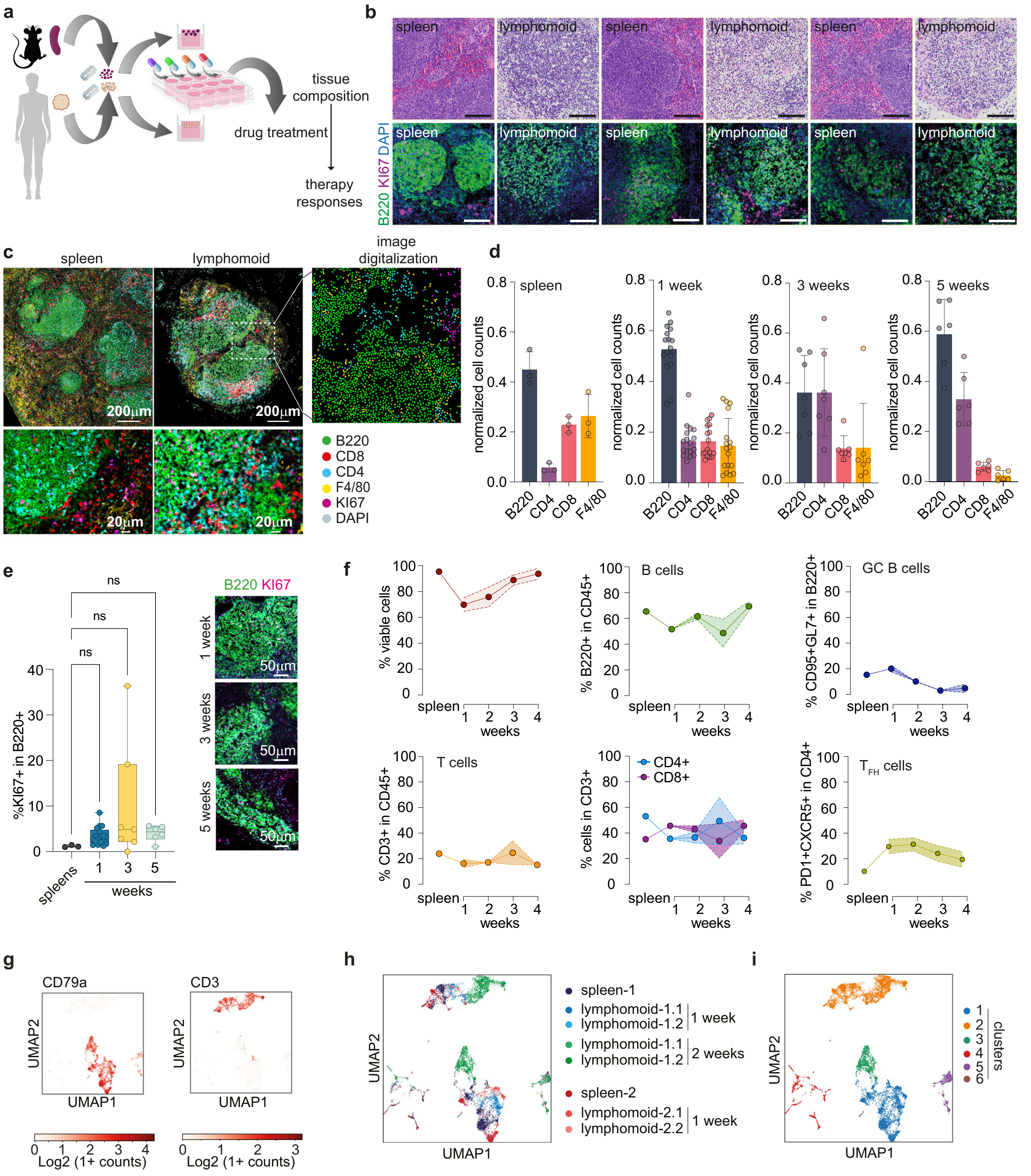

(Fig. 1i). Cluster 1 grouped B-cells from the two original spleens and from lymphomoids maintained in culture for 1 week, while cluster 3 grouped B-cells from lymphomoids in culture for 2 weeks (Fig. 1i and Supplementary Fig. 3a), suggesting that the expression profile of B-cells in lymphomoids started to change after 1 week in culture. To better define different B and T-cell subtypes in the original spleens and lymphomoids, we used a curated list of genes as markers to distinguish specific cell types (Supplementary Table 2)[48]. Interestingly, the distribution of different cell populations was similar between the original tissues and lymphomoids maintained in culture for 1 week (Supplementary Fig. 3a), indicating that they retained similar expression patterns and cellular composition. Conversely, after 2 weeks in culture, lymphomoids were enriched in B-cells expressing plasma cell markers (Supplementary Fig. 3b). Indeed, differential expression analyses between B-cells from lymphomoids in culture for 1 or 2 weeks showed upregulation of late B-cell differentiation markers such as *Xbp1* and *Zbp1*[49,50], and downregulation of early B-cells differentiation markers such as *Ebf1*, *S1pr1*, and *Pou2f2*[51–53] (Supplementary Fig. 3c). However, despite this initial transcriptional shift, we did not detect major changes in the expression of differentiation markers on the B-cell surface (e.g., CD138+ cells) (Supplementary Fig. 3d). Overall, morphological, cytological, and molecular

Fig. 1 | A system to maintain lymphoma biopsy ex vivo. a Schematic of the procedure to process and test sensitivity to therapies for murine and human samples (created with Adobe Illustrator). **b** Hematoxylin and eosin staining of a vavP-Bcl2 mouse spleen and a representative lymphomoid derived from the same spleen (upper images), and B220 + KI67 immunofluorescence of 3 independent lymphomoids (lower images) from 2 vavP-Bcl2 mice (49 weeks old and 58 weeks old). Scale bar 100 µm. **c** Representative images of 5-color immunofluorescence staining for the indicated markers of a 49 weeks old vavP-Bcl2 mouse spleen and a lymphomoid derived from the same spleen at two different resolutions and a digitalized image for the lymphomoid as a magnified cropped detail. **d** Quantification of different cell types based on fluorescence signal at different time points (the data points represent different lymphomoids and sections from 3 independent vavP-Bcl2 mice aged 47, 49, and 58 weeks old; spleen $n = 3$, lymphomoid sections $n = 17$ for 1 week, $n = 7$ for 3 weeks, $n = 6$ for 5 weeks). Data are presented as mean values +/− SD. **e** Quantification of fluorescence signal to detect proliferating B-cells at different time points (3 independent vavP-Bcl2 mice aged 47, 49, and 58 weeks old; lymphomoid sections $n = 17$ for 1 week, $n = 7$ for 3 weeks, $n = 6$ for 5 weeks). Data are shown in box and whiskers (min to max) with all data points, where the center represents the median, and were analyzed by Kruskal–Wallis followed by Dunn's posthoc test with correction for multiple comparisons using hypothesis testing. **f** Quantification of different cell types by flow cytometry of vavP-Bcl2 mouse lymphomoids at different time points (39 weeks old mouse; $n = 4$ lymphomoids for each time point; the data is plotted as the mean and error, which represents the SD). **g**–**i** UMAP projection of single cells RNA-sequencing cells color coded for cells expressing CD79a or CD3 genes (**g**), color coded by the origin of the samples (2 independent vavP-Bcl2 spleens from mice aged 43 and 47 weeks old, and $n = 4$ lymphomoids 1 week, and $n = 2$ lymphomoids 2 weeks) (**h**), color coded based on the different cell clusters found in the analysis (**i**). Source data are provided as a Source data file.

characterizations indicate that lymphomoids retain the features of the original tissue for up to 1 week in culture, defining this as the ideal time frame to use this model.

Human lymphomoids retain the cell heterogeneity of lymphoma tissues

To assess if explants could be derived from different human lymphoma subtypes, we generated and characterized lymphomoids from fresh human biopsies obtained from 27 cases of suspected lymphoma. Part of the tissues was rapidly processed to create lymphomoids and the remaining tissue was fixed and used for comparative analyses. We retrospectively retrieved available clinical information for these patients confirming lymphoma diagnosis, subtype classification, and genomic alterations (Supplementary Data 1). This cohort included ten diffuse large B-cell lymphomas, five primary mediastinal B-cell lymphomas, two high-grade B-cell lymphomas, two small lymphocytic lymphomas, one mantle cell lymphoma, one marginal zone lymphoma, three follicular lymphomas, one transformed follicular lymphoma, one Burkitt lymphoma, and one T-cell lymphoma (Fig. 2a). The lymphomoids obtained from these biopsies were maintained in culture for 3 to 7 days, and for each patient, they were treated with different drugs (Fig. 2a). First, we assessed the morphological quality of lymphomoids by histopathology analyses (hematoxylin and eosin, H&E staining) compared to the original tissue. Initial analyses revealed that twenty-one biopsies were of high quality, three samples suffered from mechanical trauma during the surgical procedure or were poorly preserved, two samples were mainly fibrotic (patients 4 and 7) and the lymphomoids obtained from one sample were rapidly contaminated with fungi (patient 5), probably because the biopsy was obtained through the oral cavity (Supplementary Fig. 4a). Among the twenty-one good-quality tissues, lymphoma cells could be detected in nineteen samples, while two samples (LP3 and LP10) contained mostly reactive lymph node tissue (Supplementary Fig. 4b). We analyzed the cell composition of lymphomoids originating from these tissues over multiple sections by multicolor fluorescent imaging using CD20 for B-cells, CD8 and CD4 to distinguish T-cells, CD68 for macrophages, and Ki67 for proliferation (Fig. 2a, b and Supplementary Fig. 4c). We compared the proportions of cells in the different subpopulations in multiple untreated lymphomoids obtained from the tumors and reactive lymph nodes with the original tissue and we observed a significant correlation for each cell type (Fig. 2c, d, and Supplementary Fig. 4b, c). In addition, we computed a similarity index considering all cell types together (non-proliferating CD20 + B-cells, proliferating CD20 + B-cells, CD4 + T-cells, CD8 + T-cells, CD68+ macrophages, other cells) for each tumor sample and lymphomoid. In general, lymphomoids are significantly more similar to their original tumor than to other tumors, and lymphomoids from the same tumor are more similar to each other than to lymphomoids originated from another tumor (Fig. 2e). Importantly, lymphomoids from the same tumor are as similar to each other as they are with the tumor from which they were derived. To further characterize the spatial and molecular structure of human lymphomoids and their tissue of origin, we performed spatial transcriptomics analyses on original tissues and lymphomoids obtained from patient 8 and patient 3 using the 10x Genomics Visium technology. The original tissue obtained from patient 8 showed that lymphoma cells were ubiquitously spread in the tissue and mixed with other cell types (Fig. 2f). In addition, we distinguished areas enriched with densely clustered lymphoma cells (red line), stroma (green line), and blood vessels (blue line) (Fig. 2f). The tissue obtained from patient 3 contained reactive follicles surrounded by areas with sinus histiocytosis and blood vessels, but not lymphoma (Supplementary Fig. 5a). Spatial transcriptomics analyses allowed to assay the full transcriptome in multiple 'spots' regularly interspersed across the tissue, each containing 20–25 cells (Supplementary Fig. 5b, c).

To overcome the lack of single-cell resolution, we used the BayesPrism method to predict the cell type composition of each spot and deconvolve spatial transcriptomics data into cell type-specific mRNA expression matrices[54]. To this purpose, we generated a reference dataset using single-cell RNA-seq data from 37 normal cell types and subtypes obtained from secondary lymphoid organs[55] and one DLBCL patient[56]. Then, we applied BayesPrism to predict the proportions of these 38 cell types in each spot (Supplementary Data 2). Importantly, with this approach, we could identify multiple spots with a high proportion of tumor cells in patient 8, but not in patient 3, in agreement with the histological classification (Fig. 2g and Supplementary Fig. 5d). Next, we unbiasedly clustered the spots based on their cell type proportions, independently on patient 8 and patient 3, and identified 5 clusters in patient 8 and 6 clusters in patient 3 (Fig. 2h and Supplementary Fig. 5e). In patient 8, the spots in clusters 3 and 5 were enriched in characteristic lymphoma cell types: proliferating B-cells, CD4+ Tfh cells, and GC B-cells. Notably, cluster 5 overlapped with the area enriched for lymphoma cells identified by histological analyses (Fig. 2f–h). Spots in clusters 2 and 4 were predominantly composed of monocytes, macrophages, and endothelial cells, while cluster 1 comprised spots with mixed cell type composition (Fig. 2i). In patient 3, areas annotated with reactive lymph nodes by histology were grouped in one cluster (cluster 4), which included GC B-cells, CD4 Tfh cells, and follicular dendritic cells; spots in cluster 2 were mainly composed of macrophages, endothelial cells, and T follicular reticular cells; cluster 0 included different groups of activated B-cells and B cells with high expression of interferon-induced genes (B IFN); and spots in cluster 1 were enriched in proliferating B-cells, plasma cells, and tumor cells, although the tumor score in this sample was low (Supplementary Fig. 5f). Thus, this spatial transcriptomics analysis led to the identification of spatial cell niches, which matched with the histological assessment of the tissue. Next, to determine if the same niches were present in six different lymphomoids derived from patient 8 maintained in culture for 3 days, we deconvolved the expression profile of each spot using

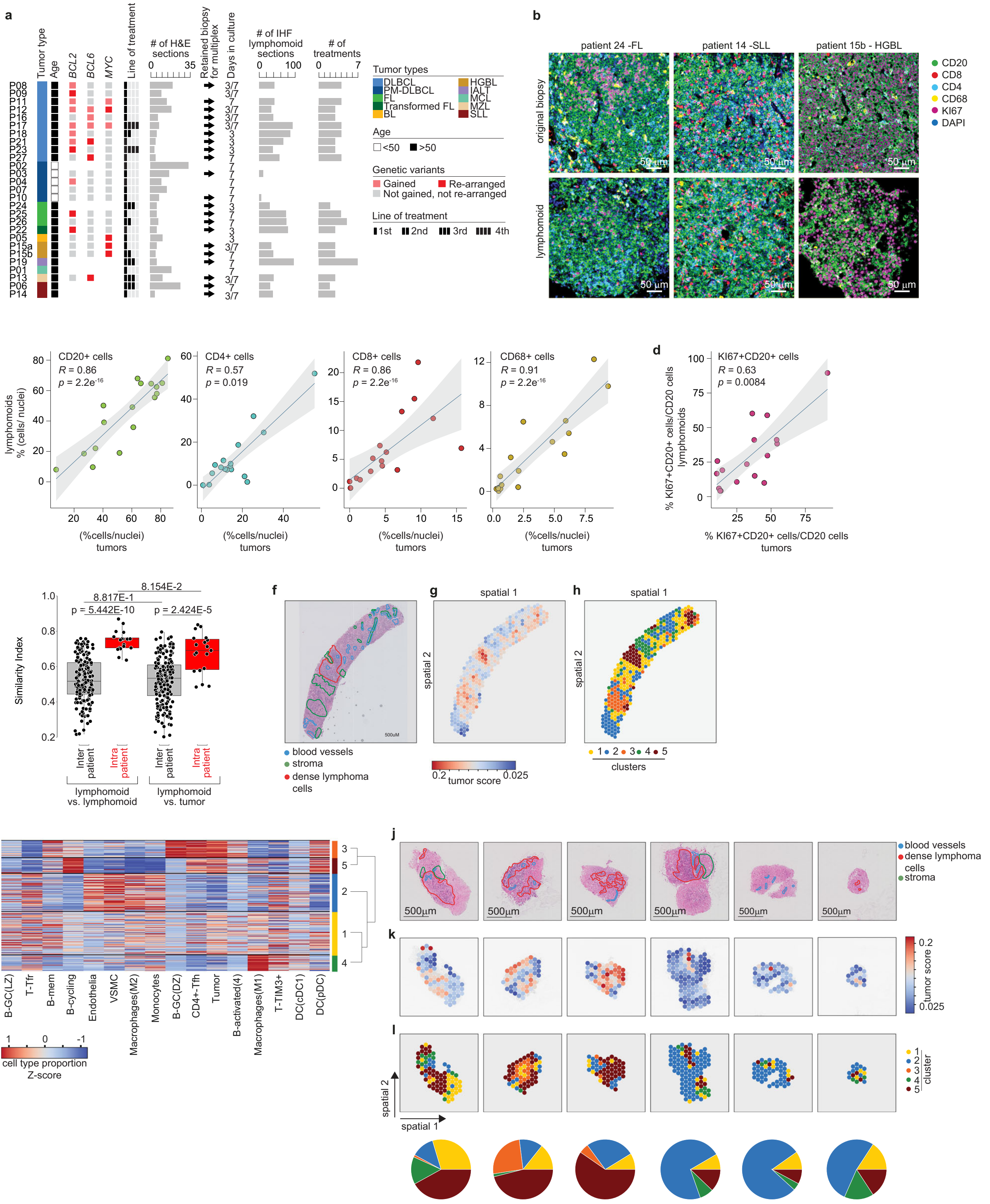

BayesPrism, and based on their cell type proportion they were assigned to one of the 5 clusters determined in the original tissue. Interestingly, each lymphomoid preserved the heterogeneity of the original tissue with spots enriched for tumor cells being observed in all lymphomoids (Fig. 2i) and all 5 clusters being recapitulated in different proportions (Fig. 2l). Overall, both multicolor imaging and spatial transcriptomics analyses confirmed that it is possible to maintain human lymphomoids in culture for a few days, while preserving the heterogeneity of the original tissue composition and the proliferation of tumor cells.

Human lymphomoids can be used to test sensitivity to different compounds

Different therapies have been approved as second-line treatments for lymphoma patients, but the efficacy of these molecules is variable across subtypes and patients. Hence, we assessed the possibility of using lymphomoids to screen in parallel multiple small molecule inhibitors and evaluate patient-specific tumor sensitivity. Multiple lymphomoids obtained from 16 different patients (6, 8, 11–14, 16–18, 21–27) were treated with ibrutinib (BTK inhibitor), idelalisib (PI3Kδ

Fig. 2 | Characterization of human lymphomoids obtained from fresh tumor biopsies. a Graphical summary of all the cases collected in this study. **b** Representative images of multicolor immunofluorescence staining of indicated markers of three human lymphoma biopsies (upper panel) and their respective lymphomoids (lower panel). Scale bar 50 µm. **c** Spearman's correlation coefficient (two-sided) analyses of untreated lymphomoids vs original tumor biopsies on the different markers analyzed by multiplex IHF ($n = 17$ B-cell lymphomas; one tumor was excluded from this analysis since it was CD20 negative). The data is shown as a percentage and was normalized to the total number of nuclei detected in each section. The graphs show the regression line and the confidence interval at 95%. **d** Spearman's correlation coefficient (two-sided) analyses of untreated lymphomoids vs original tumor biopsies on proliferating CD20+ cells analyzed by multiplex IHF ($n = 17$ B-cell lymphomas). The data is shown as percentage and was normalized to the total number of CD20+ cells in each section. The graph shows the regression line and the confidence interval at 95%. **e** Similarity index comparisons in the indicated conditions (N inter = 171, N intra = 19 for both lymphomoid-lymphomoid, and lymphomoid-tumor, originated from a total of $n = 399$ lymphomoid image acquisitions and $n = 85$ tumor image acquisitions). The data are shown as boxplots where the upper and lower hinges represent the 25th and 75th percentiles and the center is the median, and were analyzed using the Wilcoxon rank-sum test two-sided with multiple hypothesis correction using the Benjamini–Hochberg procedure. **f** H&E staining of patient 8 DLBCL biopsy. Tissue features are highlighted with lines of different colors. **g**, **h** Representation of 10X Genomics Visium spots color-coded by the tumor score (**g**) and based on unbiased clustering (**h**). **i** Heatmap of cell type enrichment in each spot of the biopsy determined using Bayesprism deconvolution. Only top 4 differentially enriched cell types in each cluster are shown. The cell state proportions are z-scale normalized for each cell type. The dendrogram shows the distances between the different clusters. **j** H&E staining of six lymphomoids maintained in culture for 3 days. Tissue features are highlighted with lines of different colors. Scale bar 500 µm. **k**, **l** Representation of 10X Genomics Visium spots color-coded by the tumor score (**k**), based on cluster scores obtained in the original tissue (l-top), and pie-charts summarizing the cluster composition of each lymphomoid (l-bottom). Source data are provided as a Source data file.

inhibitor), lenalidomide (E3 ubiquitin ligase modulator), venetoclax (BCL2 inhibitor), or tazemetostat (EZH2 inhibitor). Lymphomoids from two independent and sequential biopsies (LP15A and LP15B) of an early relapsed case of high-grade B-cell lymphoma were treated with alisertib (Aurora kinase A inhibitor), everolimus (mTOR inhibitor), and lenalidomide. Lastly, lymphomoids from a T-cell lymphoma were treated with panobinostat (HDAC inhibitor), 5-azacytidine (methyltransferase inhibitor), tazemetostat, idelalisib, alisertib, lenalidomide, and venetoclax. The efficacy of these treatments was determined based on the difference of proliferating B-cells (fold change) that was detected in treated vs. untreated samples (Fig. 3a–c). This analysis revealed heterogeneous responses to the same or different compounds among patients (Fig. 3b). For instance, lymphomoids derived from patient 8 were exclusively sensitive to ibrutinib, while lymphomoids derived from patient 21 were only sensitive to idelalisib, and those from patients 12, 14, 17, 18 showed similar sensitivity to both ibrutinib and idelalisib (Fig. 3b). In addition, to distinguish between cytotoxic and cytostatic effects, we computed the fold change of total B-cells between treated and untreated conditions (Fig. 3c). In general, we observed lower fold changes for proliferating B-cells compared to the total number of B-cells, suggesting that mainly B-cell proliferation was affected by these treatments (Fig. 3b, c). Nonetheless, we also observed a concomitant reduction of total and proliferating B-cells upon treatment with ibrutinib, idelasilib, and venetoclax in multiple patients, suggesting that these drugs may also exert cytotoxic effects. For patient 15, we obtained two sequential biopsies taken 7 months apart, before and after tumor relapse (LP15A and LP15B, respectively). Lymphomoids derived from this patient were treated with the same compounds and showed similar sensitivity to everolimus and alisertib, but not to lenalidomide. Interestingly, whereas in the first biopsy (L15A) the effect was largely cytostatic, in the second biopsy (L15B) we observed cytotoxic effects (Fig. 3b, c and Supplementary Fig. 6a, b). We also compared the effect of 3 or 7 days of treatment on lymphomoids derived from 5 different patients, but we did not observe major differences (Supplementary Fig. 7). Next, we used spatial transcriptomics analyses to assess sensitivity or resistance to targeted therapies based on the estimated proportion of tumor cells, and to understand the effect of these therapies not only on tumor cells but also on the tumor microenvironment composition. The proportion of tumor cells in lymphomoids obtained from patient 8 treated with ibrutinib and idelalisib confirmed sensitivity to ibrutinib but not idelalisib (Fig. 3d). Indeed, clustering of spots based on gene expression in untreated and treated lymphomoids showed that ibrutinib-treated lymphomoids formed a distinct cluster (cluster 4) while clusters 1 and 2 were composed of both untreated and idelalisib-treated samples (Fig. 3e). Importantly, in ibrutinib-treated lymphomoids, we noticed upregulation of several inflammatory genes (e.g., *IFI27*, *IFI6*, *IFIT3*) and loss of expression of B-cell markers (Fig. 3f), indicating that ibrutinib affected viability and proliferation of B-cells and triggered the activation of inflammatory anti-tumoral responses. Next, to decipher if these compounds affected different subpopulations of the tumor microenvironment, we compared the proportion of different cell populations in untreated and treated lymphomoids. In lymphomoids treated with ibrutinib, we detected a strong reduction of tumor cells, GC B-cells, and proliferating B-cells, and an increase of CD8+ cytotoxic T-cells and macrophages (Fig. 3g and Supplementary Table 3). Conversely, in the idelalisib-treated lymphomoids, the proportion of tumor cells was largely unchanged, but GC B-cells, CD4+ Tfh cells, and FDC were enriched, and proliferating and activated B-cells were depleted (Fig. 3g), indicating that treatment with idelalisib, although not effective on tumor cells, was influencing normal B-cells. Hence, lymphomoids represent a valid method to test in parallel the activity of different therapies and, in combination with spatial analyses of the tissue, they could reveal how the tumor microenvironment reacts to drug treatment.

Compare the effect of small molecules ex vivo and in the clinic

To assess if the sensitivity to therapy observed ex vivo using lymphomoids matched clinical responses, we retrieved treatment response data for 7 patients among our donors. These cases were treated with the same compounds that were tested in lymphomoids derived from their original tumor. Two patients diagnosed with SLL (patient 6 and patient 14) were treated with either a combination of obinutuzumab (anti-CD20 antibody) and acalabrutinib (BTK inhibitor), or acalabrutinib alone (Fig. 4a, b). Although we did not test combination therapies, in patient 6- and patient 14-derived lymphomoids (LP06 and LP14, respectively), we observed a significant reduction of proliferating B-cells when treated with ibrutinib, with complete depletion of proliferating B-cells in LP06 (Fig. 4a) and a residual 10% of proliferating (KI67+) B-cells in LP14 (Fig. 4b). Consistently, in the clinic these patients showed either complete (patient 6) or partial (patient 14) response (Fig. 4a, b). Patient 11 was diagnosed with DLBCL and treated with rituximab (anti-CD20 antibody) and lenalidomide as an alternative to chemotherapy. Lymphomoids obtained from the tumor biopsy showed that the tumor was refractory to lenalidomide (Fig. 4c). Consistently, after 2 cycles of treatment, radiological assessment by PET-CT showed no metabolic response (NMR) with an overall disease progression (Deauville score 5) for patient 11 (Fig. 4c). A second patient diagnosed with R/R DLBCL (patient 17) was initially treated with ibrutinib and subsequently with tafasitamab (anti-CD19) and lenalidomide. Both treatments resulted in NMR with a Deauville score of 5 (Fig. 4d). Lymphomoids derived from this patient (LP17) were treated with lenalidomide and ibrutinib. Although they exhibited sensitivity to ibrutinib, they confirmed the resistance to lenalidomide (Fig. 4d).

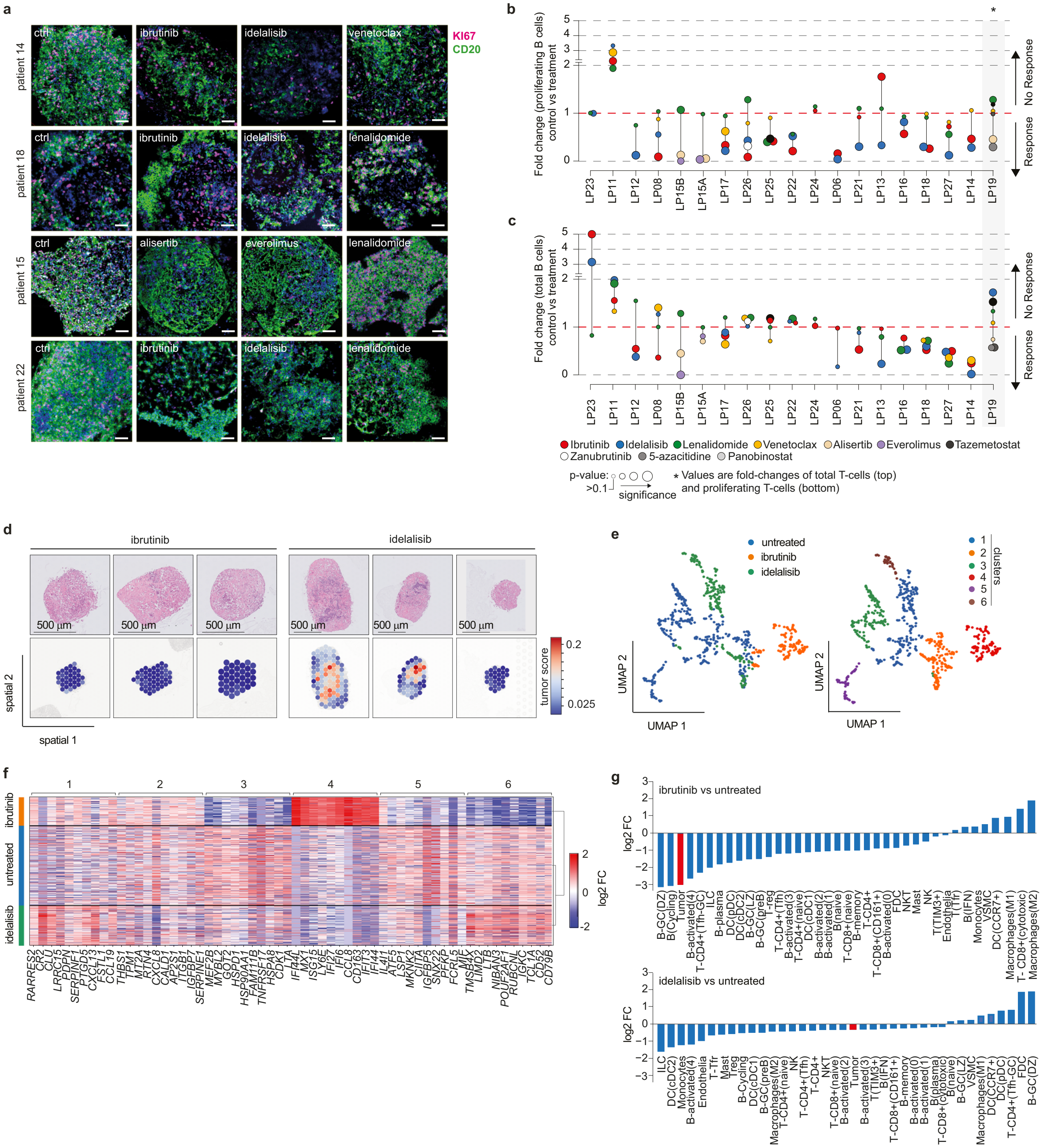

Fig. 3 | Sensitivity to targeted therapies using patient-derived lymphomoids. **a** Representative images of immunofluorescence staining for KI67 and CD20 in lymphomoids derived from 4 different biopsies. Scale bar 50 µm. **b**, **c** Weighted ratios of proliferating CD20+ cells (**b**) and total CD20+ cells (**c**) compared to untreated controls. Each treatment is color-coded and the *p*-values were calculated using non-parametric ANOVA followed by Dunn's test (two-sided) with *p*-value adjustment using Bonferroni's correction. **d** H&E and tumor score of ibrutinib and idelalisib-treated lymphomoids. **e** UMAP projection of 10X Genomics Visium spots colored by sample (left) and by cluster (right). **f** Heatmap of differentially expressed genes in each cluster and sample obtained in the 10X Genomics Visium experiment. **g** Comparison of cell type enrichment in ibrutinib (top) and idelalisib (bottom) treated lymphomoids versus control. Source data are provided as a Source data file.

Patient 18, another patient with R/R DLBCL was treated with ibrutinib and at the baseline PET-CT showed a complete metabolic response (CMR) following 3 weeks of ibrutinib monotherapy. Similarly, ibrutinib led to a significant reduction of proliferating B-cells, confirming sensitivity to this molecule (Fig. 4e). Patient 13 was diagnosed with relapsed MZL and was treated with ibrutinib, but the treatment was interrupted after 3 weeks due to severe bleeding, and the PET-CT showed tumor progression. Thus, the treatment was switched to a combination of tafasitamab and lenalidomide, but the tumor did not respond (Fig. 4f). Because ibrutinib had only been given for a short period and had demonstrated high efficacy in clinical trials with MZL patients[57], patient 11 was treated again with ibrutinib, but the tumor remained refractory to this treatment as confirmed by PET-CT with NMR and a Deauville score of 5 (Fig. 4f). Lymphomoids obtained from

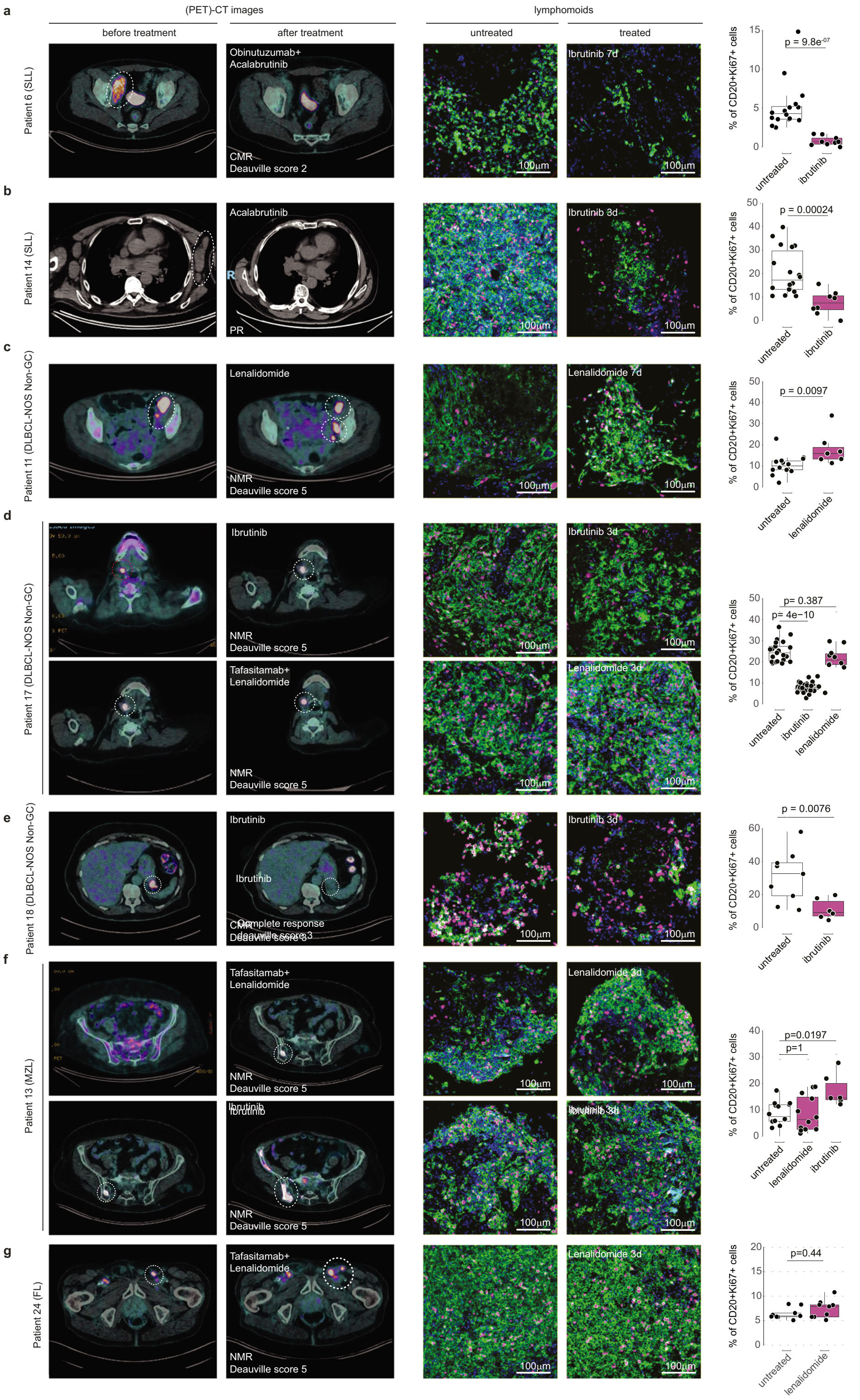

Fig. 4 | Matched results obtained in the clinic and on lymphomoids in seven patients. a–f PET-CT before and after treatment, representative image and quantification (of the CD20 and KI67 immunofluorescence signal of the lymphomoids derived from patient 6 (**a**, ctrl $n = 16$; ibrutinib $n = 9$), patient 14 (**b**, ctrl $n = 18$; ibrutinib $n = 8$), patient 11 (**c**, ctrl $n = 14$; lenalidomide $n = 7$), patient 17 (**d**, ctrl $n = 21$; ibrutinib $n = 33$, lenalidomide $n = 10$), patient 18 (**e**, ctrl $n = 44$, ibrutinib $n = 12$), patient 13 (**f**, ctrl $n = 14$; ibrutinib $n = 6$, lenalidomide $n = 12$), and patient 24 (**g**, ctrl $n = 9$; lenalidomide $n = 9$). The data are shown as boxplots where the upper and lower hinges represent the 25th and 75th percentiles and the center is the median, and were analyzed by either two-sided Wilcoxon rank-sum test or Kruskal–Wallis followed by Dunn's posthoc test. CMR complete metabolic response, NMR no metabolic response, PR partial response. Source data are provided as a Source data file.

the relapsed tumor (LP13) were treated with ibrutinib and lenalidomide, but neither compound was effective, consistent with the observed clinical response. Finally, patient 24 was diagnosed with relapsed follicular lymphoma and treated (3rd line) with tafasitamab and lenalidomide, but after two cycles the PET-CT revealed that the lesions did not respond to the treatment (Fig. 4g). Likewise, lymphomoids from the same patient did not exhibit sensitivity to lenalidomide.

Overall, although in lymphomoids we only tested sensitivity and resistance to targeted therapies and immunomodulatory agents and did not include combination treatments with monoclonal antibodies like rituximab, treatments measured in lymphomoids largely matched the patients' response.

Discussion

The efficacy of anti-cancer treatments depends on multiple parameters, which can be evaluated by personalized medicine approaches in order to ultimately tailor medical treatments to individual patients. However, to fulfill this promise, predictive models of each tumor are required to assess treatment response. In the past years, we have witnessed the emergence of different models based on cell lines, patient-derived xenografts, organoids, and tissue explants that could be suitable to test response to therapies[56,58–60]. For example, in a number of solid tumors and follicular lymphoma, sensitivity to immunotherapies has been tested in dissociated tissue biopsies[16,19]. However, the majority of these models do not preserve the tissue composition and its spatial organization. Lymphomoids generated from non-disaggregated tissue biopsies overcome these limitations and could represent a reliable alternative to rapidly test sensitivity to different therapies, although long-term responses cannot be assessed in this system. In lymphomoids, measuring proliferating B-cells could be sufficient to identify the most effective targeted therapy treatment. Interestingly, the analysis of lymphomoids from two independent biopsies taken 7 months apart on a high-grade B-cell lymphoma patient that relapsed after being treated with chemotherapy revealed that they were still sensitive to the same compounds. These results suggest that in tumors in which the cell composition is retained, ex vivo models could be used to anticipate the effect of inhibitors also of the relapsed tumor. However, to determine the clinical impact of our approach, prospective trials with matching therapies need to be designed. Ideally, lymphomoids could be used in clinical trials where patients will be enrolled based on specific inclusion criteria with a predefined clinical endpoint. In addition, it could be interesting to include combination therapies with monoclonal antibodies, although their efficacy and selection criteria are well established in the clinic. Indeed, some patients in our study received monoclonal antibodies such as rituximab together with the targeted therapies. Nevertheless, our system is currently designed to test the effect of therapies on tissue-resident cells, while immunotherapies often relies on the recruitment of circulating immune cells. For these reasons, we did not add combinatorial treatments in our assays.

Despite this limitation, we have reported that in 8 out of 9 cases sensitivity to specific therapies in lymphomoids matched with clinical responses. While these results are promising, additional samples are required to establish the robustness and reliability of our approach.

In parallel to their preclinical application, the lymphomoids could serve as a system to understand tissue remodeling after treatment using spatially resolved molecular assays. The initial analyses that we performed revealed rearrangements in the tissue organization and immune cell subpopulations upon treatment. Interestingly, we noticed that treatment with ibrutinib induced an inflammatory response and enrichment of activated CD8+ T cells, macrophages, and dendritic cells (*CCR7*+). This opens the possibility of directly studying immune cell activation and their functional interdependency using lymphomoids. In addition, it is possible to envision that lymphomoids could be generated from normal lymph nodes and they could serve as an alternative method to the self-organizing lymphoid tissue system that has been recently proposed[61]. Overall, lymphomoids represent a technology to study therapy response preserving the tissue architecture and the role of the tumor microenvironment, and eventually could be used to model individual patient tumors and treatment response.

Methods

Human sample collection

Patients with a clinical suspicion of abdominal or axillary lymphoma and scheduled for a surgical or needle lymph node biopsy were informed about the project and offered to participate in the study. Upon written informed consent, fresh biopsies from lymphoid tissue were collected in 50 ml Falcon tubes containing 30 mL of cold PBS + 1x normocin. The samples were then immediately transported on ice inside a polystyrene box to the lab, where they were processed as described below. All procedures were carried in accordance with the Ordinance on human research with the exception of Clinical trials (HRO) and were previously approved by the *Commission cantonale d'éthique de la recherche sur l'être humain* (CER-VD, project-ID 2020-02532). Participation in this study was completely voluntary and non-compensated. Sex and age were not considered in this study.

Animal models

vavP-Bcl2 (C57BL/6J) mice were bred and housed in ventilated cages in the conventional mouse husbandry of EPFL, with dark/light cycles of 12 h, a temperature of 22 °C ±, and a humidity of 55% ± 10. Sex was not considered in this study, and both males and females were used. The mice were monitored on a routine basis 3 times a week and they were euthanized if they showed any signs of discomfort or pain as determined using a score sheet to assess appearance, body condition, locomotion/behavior, difficulties to breath and tumor development (abdominal dilatation or mass). Abnormal abdominal expansion was also a criteria for withdrawal. The mice were euthanized at the timepoints described in the manuscript and therefore no endpoint was exceeded. All the experiments were carried out in accordance with the Swiss Animal Welfare Regulations and were previously approved by the Cantonal Veterinary Service of the Canton de Vaud (license VD3631).

Tissue culture

Tumor tissues were placed in PBS and rapidly processed with a McIlwain Tissue Chopper (Ted Pella Inc.) producing fragments of 0.75–1.5 mm^3. Four to ten explants were picked randomly and then placed in inserts with permeable, membranous bottom (Millicell-CM, Millipore) containing a 1:1 solution of Vitrogel RGD High Concentration (TheWell Bioscience) and RPMI1640 supplemented with 5% FBS, 1x normocin, 1x insulin/selenium/transferrin, and 1x sodium pyruvate. The insert was placed in a 12-well plate and left in a 5% CO_2 incubator at 37 °C for 20 min for the matrix to gelify. Finally, RMPI1640 complete + 0.2 µg/ml hBAFF (Biolegend) was added to each well. Small molecule inhibitors were added at the following concentrations: ibrutinib (2 µM), zanubrutinib (1 µM), idelalisib (10 µM), lenalidomide (10 µM), panobinostat (0.5 µM), venetoclax (1 µM), alisertib (50 nM), everolimus (100 nM), tazemetostat (1 µM), 5-azacytinide (5 µM). Media was replaced every 3–4 days.

Hydrogel rheology

The rheological properties of the gel were tested using a Malvern Kinexus Pro+ dynamic rheometer (Malvern Panalytical, UK) at a 0.1% controlled shear rate model, with a 20 mm parallel-plate rough surface geometry. Samples were prepared by mixing the VitroGel RGD hydrogel with RPMI 1640 medium at the following dilution factors: 1:2 (one part gel, one part medium), 1:5 (one part gel, 4 parts medium) and 5:1 (4 parts gel, one part medium). For final gel strength tests, 1200 µl VitroGel RGD and RPMI 1640 medium mixture at 1:1, 1:5, and 5:1 were prepared in a 35 mm petri dish. The mixture was allowed to stabilize at room temperature for 30 min, and then 1200 µl of RPMI 1640 medium was added on the surface of the hydrogel. The hydrogels were incubated at 37 °C for 24 h, and then the cover medium was removed before the final gel testing. Ten-minute single-frequency oscillation time sweeps were performed using the rheometer at a 0.1% controlled shear rate model with a 20 mm parallel-plate rough surface geometry.

Immunostaining

Formalin-fixed paraffin-embedded (FFPE) tissues were sectioned at 5 µm in a Hyrax M25 microtome and placed in Superfrost™ slides. 5-plex immunohistofluorescent staining was performed on the fully automated Ventana Discovery Ultra (Roche Diagnostics) using the manufacturer's solutions and antibodies. Briefly, deparaffinized and rehydrated FFPE sections were pretreated with heat using standard conditions (40 min) in CC1 solution. Primary antibodies (human): CD4 (SP35), CD8 (SP57), CD20 (L26), CD68 (KP-1), KI-67 (30-9), all of them ready-to-use. Primary antibodies (mouse): B220, CD4, CD8, F4/80. The images were acquired in an Olympus VS120 whole slide scanner and analyzed using QuPath.

Image digitalization and analysis

The image analysis pipeline is based on QuPath[62], DeepCell[63], MCMICRO[64], and custom scripts implemented in Groovy, Python and RSource code and software dependencies can be found under https://doi.org/10.5281/zenodo.14011651. Briefly, .vsi images acquired on the Slide Scanner (Olympus), were opened as a project on QuPath. First, lymphoid boundaries were drawn and exported using a custom script. Then, the fluorescence thresholds for each channel were calibrated in each image and exported using a second script. Next, the images were converted to .ome.tiff and DeepCell was run to detect the nuclei and the cytoplasmic areas, which were used for marker quantification of the nuclear and cytoplasmic markers, respectively. Marker quantification was performed using MCMICRO by taking, for each cell, the mean intensity of each marker within the respective segmentation mask. Finally, a cell was classified as positive for a given marker if the difference between the cytoplasmic intensity of that marker and its calibrated threshold was the highest across markers. Cells with intensities below all marker thresholds are deemed as coming from an unknown cell type and called otherCell. In addition, cells assigned to markers are further classified as proliferating or not according to whether their nuclear Ki67 intensity is above or below its calibrated threshold. Lymphomoid-level cell composition is obtained by intersecting the spatial coordinates of classified cells with the lymphomoid boundaries saved at the first step.

Flow cytometry

Spleens, lymph nodes, and lymphomoids were mechanically disaggregated, filtered through a 70 µm nylon mesh strainer and resuspended in cold FACS buffer (2% FBS, 1 mM EDTA in PBS). Erythrocytes were lysed using a Red Blood Cell Lysis buffer (Biolegend) for 2 min at room temperature and then cells were washed in PBS and incubated for 15 min at room temperature with a PBS solution containing the fixable viability dye Zombie Violet™ (Biolegend, 1:100) and CD16/CD32 Fc Block (BD Biosciences, 1:100). Next, cells were washed and stained with the following fluorescent-labeled antibodies for 30 min at 4 °C: Biolegend: CD3e-FITC (145-2-C11, 1:300), CD4-AF700 (RM4-5, 1:300), CD8-BV570 (53-6.7, 1:200), CXCR5-PerCP-Cy5 (L138D7, 1:300), PD1-PECy7 (29F.1A12, 1:300), CD95-PE (SA367H8, 1:200), CD138-PE-Cy7 (281-1, 1:300); BD Pharmingen: CD45-APCCy7 (30-F11, 1:500), T- and B-cell activation antigen-AF647 (GL7, 1:200); BD Horizon: B220-PECF594 (RA3-6B2, 1:500). Finally, cells were washed, fixed in BD Cytofix/Cytoperm Solution (BD Biosciences), washed again and analyzed in a Gallios machine (Beckman Coulter). Data was analyzed using FlowJo 10.8 (Becton Dickinson).

Single-cell RNA sequencing and data processing

vavP-Bcl2 spleens and lymphomoids were mechanically disaggregated, filtered through a 70 µm nylon mesh strainer and resuspended in PBS. Erythrocytes were lysed using a Red Blood Cell Lysis buffer (Biolegend) for 2 min at room temperature and then cells were washed in PBS, resuspended in medium and processed for sequencing using the SingleCell 3' Reagent Kit v3.1 and a 10x Chromium single cell controller. The sequencing depth was between 183 to 225 million reads/sample. Raw sequencing reads were aligned to mouse reference genome GRCm38 using 10x Cell Ranger pipeline v6.0.2. Count matrices were further processed in Python v3.9.1 using Scanpy v1.9.1 toolkit. Cells with less than 200 genes expressed, and genes detected in less than 3 cells were removed. For the first murine tumor and lymphomoids, cells with total counts between 2000 and 75,000 expressed genes between 800 and 5000, and counts from mitochondrial genes under 10% were retained. For the second tumor, cells with total counts between 2000 and 100,000, counts from mitochondrial genes under 15%, and between 1000 and 8000 total genes expressed were shortlisted. The two parental tumor samples and corresponding lymphomoids counts matrices were concatenated. Merged counts were normalized for total 100,000 counts per cell, and log transformed. Top 2000 highly variable genes were used to construct a UMAP projection of the cells with top 50 principal components, 15 neighbors and 0.2 as the effective minimum distance (min_dist parameter). Finally, Leiden clustering algorithm was used with 0.1 resolution to obtain 6 clusters.

Spatial transcriptomics

Tissue and slide preparation. Formalin-fixed paraffin-embedded (FFPE) tissues were sectioned at 5 µm in a Hyrax M25 microtome and placed in a Visium slide. The slides were then deparaffinized, stained with H&E, and images were acquired using an Olympus VS120 whole slide scanner. Next, sections were decrosslinked, and were subsequently treated as per manufacturer's instructions to hybridize the probes, ligate them, and finally generate FFPE libraries. Samples were sequenced using Illumina's NextSeq.

Spatial transcriptomics data preprocessing

For each capture area in the 10x Visium slide, FASTQ files and H&E images were processed using Space Ranger v1.3.0. Staining images were aligned and spots covered by tissue were selected using Manual Alignment for Space Ranger wizard found in the Loupe Browser software v5.1.0. The aligned and selected spots were passed to Space Ranger call using the loupe-alignment argument. The raw reads were aligned to hg38 human reference genome (refdata-gex-GRCh38-2020-A). The aligned reads were analyzed using Python v3.9.1 using Scanpy v1.9.1 toolkit. A median of 26,062 counts was obtained, with 7080 median genes per spot.

Cell detection in Visium slides H&E images

For each capture area of the 10x Visium slide, the corresponding H&E images were processed using the inbuilt cell detection option in QuPath v0.3.2 with default parameters. The detected cell measurements (centroid, area, etc.) were exported to a tab-separated file, and an in-house R script was used to compute the number of cells identified within each visium spot.

10x Visium data deconvolution and processing

Count values for each spot of the 10x Visium slide was deconvolved using BayesPrism v2.0, using the single-cell reference dataset of the 38 cell types. The final theta values from the BayesPrism fitted object were for downstream analysis. Parental Visium spots' deconvolved signals were used to cluster the spots using Leiden clustering algorithm at 0.2 resolution. Marker cell types and marker genes for the clusters were calculated using Scanpy's rank_gene_groups function, with Wilcoxon test method.

Spot cluster annotation

Each parental cluster's mean cell type fraction value (theta values from BayesPrism output) for each cell type was calculated, and a template cell type fraction vector for each cluster was created. For each Visium spot in the untreated lymphomoid, Jennson–Shannon distance between the deconvolved cell type fraction vector and each of the 5 parental cluster templates were calculated. The spot was then attributed to that parental cluster whose template had the least distance from the spot's cell type fraction.

Similarity index

We represented the intra-tumor cell type heterogeneity of each tumor sample or control lymphomoid i with a compositional vector $C_i = [p_{i,1}, \ldots, p_{i,K}]$, with $\sum_{k=1}^{K}(p_{i,k}) = 1$, whose elements are the cell type proportions of the K cell types (non-proliferating CD20+ B cells, proliferating CD20+ B cells, CD4+ T cells, CD8+ T cells, CD68+ macrophages, otherCells) detected from the immunofluorescence image analyses. Then, we computed a Similarity Index between the compositional vectors of each pair of samples i,j as

$$SI_{i,j} = 1 - \frac{1}{2}\sum_{k=1}^{K}\left|C_i - C_j\right|$$

Finally, we computed the average SI of samples from the same patient (intra, one data point per patient and per sample type i.e., tumor or control lymphomoid) and the average SI of samples belonging to different patients (inter, one data point for each combination of patients x sample types). We tested the differences between intra and inter SI distributions computed for lymphomoids vs lymphomoids, lymphomoids vs tumors, and tumors vs tumors with Wilcoxon rank-sum test.

Statistics and reproducibility

Data were analyzed using R[65] and the GRAPHPAD PRISM software. Normality was assessed using D'Agostino-Pearson's omnibus normality test. Means were compared with two-tailed unpaired Student's t-test or Mann–Whitney's non-parametric test. One-way analysis of variance was performed to compare more than two variables. In case groups would not pass normality or data was comprised between 0 and 1, samples were analyzed using the Kruskal–Wallis test. To isolate differences between groups, the Dunn's multiple comparisons test was performed. *P*-values are indicated for each experiment. Correlation coefficients were computed dividing the sum of the values for each parameter (CD20, CD4, CD8, and CD68) by the sum of the total of cell counts, and the sum of CD20 + KI67+ by the sum of CD20 counts. Likewise, the summaries presented in Fig. 3c and d were computed on the weighted ratios comparing the values of the treated lymphomoids to the untreated ones for each patient. Mouse experiments were performed with at least 3 independent lymphomoids and the experiment was repeated with at least 2 independent mice. Error bars indicate standard deviation unless stated otherwise.

Data availability

The Visium data generated in this study have been deposited in the Gene Expression Omnibus (GEO) database under accession code GSE269695. The single-cell RNA sequencing dataset used to deconvolve spatial transcriptomics is deposited in the Gene Expression Omnibus (GEO) database under accession code GSE269695. The single-cell RNA sequencing data used in this study are available in the GEO database under accession code GSE269697. The remaining data are available within the Article, Supplementary Information, or Source data file. Source data are provided with this paper.

Code availability

Source data are provided with this paper. The image analysis pipeline can be found under https://zenodo.org/records/14011652. The remaining data are available within the Article, Supplementary Information, or Source data file.

References

1. Black, J. R. M. & McGranahan, N. Genetic and non-genetic clonal diversity in cancer evolution. *Nat. Rev. Cancer* **21**, 379–392 (2021).
2. Barroso, M. et al. A path to translation: How 3D patient tumor avatars enable next generation precision oncology. *Cancer Cell* **40**, 1448–1453 (2022).
3. Abdolahi, S. et al. Patient-derived xenograft (PDX) models, applications and challenges in cancer research. *J. Transl. Med.* **20**, 206 (2022).
4. LeBlanc, V. G. et al. Single-cell landscapes of primary glioblastomas and matched explants and cell lines show variable retention of inter- and intratumor heterogeneity. *Cancer Cell* **40**, 379–392.e9 (2022).
5. Voabil, P. et al. An ex vivo tumor fragment platform to dissect response to PD-1 blockade in cancer. *Nat. Med.* **27**, 1250–1261 (2021).
6. Broutier, L. et al. Human primary liver cancer-derived organoid cultures for disease modeling and drug screening. *Nat. Med.* **23**, 1424–1435 (2017).
7. Ganesh, K. et al. A rectal cancer organoid platform to study individual responses to chemoradiation. *Nat. Med.* **25**, 1607–1614 (2019).
8. Tiriac, H. et al. Organoid profiling identifies common responders to chemotherapy in pancreatic cancer. *Cancer Discov.* **8**, 1112–1129 (2018).
9. Yao, Y. et al. Patient-derived organoids predict chemoradiation responses of locally advanced rectal cancer. *Cell Stem Cell* **26**, 17–26.e6 (2020).
10. Khan, A. O. et al. Human bone marrow organoids for disease modelling, discovery and validation of therapeutic targets in hematological malignancies. *Cancer Discov.* https://doi.org/10.1158/2159-8290.CD-22-0199 (2022).
11. Guillen, K. P. et al. A human breast cancer-derived xenograft and organoid platform for drug discovery and precision oncology. *Nat. Cancer* **3**, 232–250 (2022).
12. Decaup, E. et al. Anti-tumor activity of obinutuzumab and rituximab in a follicular lymphoma 3D model. *Blood Cancer J.* **3**, e131 (2013).
13. Mannino, R. G. et al. 3D microvascular model recapitulates the diffuse large B-cell lymphoma tumor microenvironment in vitro. *Lab Chip* **17**, 407–414 (2017).
14. Tian, Y. F. et al. Integrin-specific hydrogels as adaptable tumor organoids for malignant B and T cells. *Biomaterials* **73**, 110–119 (2015).
15. Foxall, R. et al. Developing a 3D B cell lymphoma culture system to model antibody therapy. *Front. Immunol.* **11**, 605231 (2021).
16. Faria, C. et al. Patient-derived lymphoma spheroids integrating immune tumor microenvironment as preclinical follicular lymphoma models for personalized medicine. *J. Immunother. Cancer* **11**, e007156 (2023).
17. Shah, S. B. et al. Combinatorial treatment rescues tumour-microenvironment-mediated attenuation of MALT1 inhibitors in B-cell lymphomas. *Nat. Mater.* **22**, 511–523 (2023).
18. Araujo-Ayala, F. et al. A novel patient-derived 3D model recapitulates mantle cell lymphoma lymph node signaling, immune profile and in vivo ibrutinib responses. *Leukemia* **37**, 1311–1323 (2023).
19. Kastenschmidt, J. M. et al. A human lymphoma organoid model for evaluating and targeting the follicular lymphoma tumor immune microenvironment. *Cell Stem Cell* **31**, 410–420.e4 (2024).
20. Pasqualucci, L. & Dalla-Favera, R. Genetics of diffuse large B-cell lymphoma. *Blood* **131**, 2307–2319 (2018).
21. Dheilly, E. et al. Cathepsin S regulates antigen processing and T cell activity in non-Hodgkin lymphoma. *Cancer Cell* **37**, 674–689.e12 (2020).
22. Morin, R. D. et al. Frequent mutation of histone-modifying genes in non-Hodgkin lymphoma. *Nature* **476**, 298–303 (2011).
23. Pasqualucci, L. et al. Inactivating mutations of acetyltransferase genes in B-cell lymphoma. *Nature* **471**, 189–195 (2011).
24. Pasqualucci, L. et al. Analysis of the coding genome of diffuse large B-cell lymphoma. *Nat. Genet.* **43**, 830–837 (2011).

25. Chambwe, N. et al. Variability in DNA methylation defines novel epigenetic subgroups of DLBCL associated with different clinical outcomes. *Blood* **123**, 1699–1708 (2014).
26. Zhang, J. et al. The CREBBP acetyltransferase is a haploinsufficient tumor suppressor in B-cell lymphoma. *Cancer Discov*. **7**, 322–337 (2017).
27. Jiang, Y. et al. *CREBBP* inactivation promotes the development of HDAC3-dependent lymphomas. *Cancer Discov*. **7**, 38–53 (2017).
28. Alizadeh, A. A. et al. Distinct types of diffuse large B-cell lymphoma identified by gene expression profiling. *Nature* **403**, 503–511 (2000).
29. Lu, X. et al. PRMT5 interacts with the BCL6 oncoprotein and is required for germinal center formation and lymphoma cell survival. *Blood* **132**, 2026–2039 (2018).
30. Carbone, A. et al. Follicular lymphoma. *Nat. Rev. Dis. Prim.* **5**, 83 (2019).
31. Sehn, L. H. & Salles, G. Diffuse large B-cell lymphoma. *N. Engl. J. Med.* **384**, 842–858 (2021).
32. De Leval, L. & Jaffe, E. S. Lymphoma classification. *Cancer J.* **26**, 176–185 (2020).
33. Alaggio, R. et al. The 5th edition of the World Health Organization classification of haematolymphoid tumours: lymphoid neoplasms. *Leukemia* https://doi.org/10.1038/s41375-022-01620-2 (2022).
34. Campo, E. et al. The international consensus classification of mature lymphoid neoplasms: a report from the clinical advisory committee. *Blood* **140**, 1229–1253 (2022).
35. Chapuy, B. et al. Molecular subtypes of diffuse large B cell lymphoma are associated with distinct pathogenic mechanisms and outcomes. *Nat. Med.* **24**, 679–690 (2018).
36. Schmitz, R. et al. Genetics and pathogenesis of diffuse large B-cell lymphoma. *N. Engl. J. Med.* **378**, 1396–1407 (2018).
37. Basso, K. & Dalla-Favera, R. Germinal centres and B cell lymphomagenesis. *Nat. Rev. Immunol.* **15**, 172–184 (2015).
38. Scott, D. W. & Gascoyne, R. D. The tumour microenvironment in B cell lymphomas. *Nat. Rev. Cancer* **14**, 517–534 (2014).
39. Pangault, C. et al. Follicular lymphoma cell niche: identification of a preeminent IL-4-dependent T(FH)-B cell axis. *Leukemia* **24**, 2080–2089 (2010).
40. Amé-Thomas, P. & Tarte, K. The yin and the yang of follicular lymphoma cell niches: role of microenvironment heterogeneity and plasticity. *Semin Cancer Biol.* **24**, 23–32 (2014).
41. PDQ Adult Treatment Editorial Board. In *PDQ Cancer Information Summaries* (National Cancer Institute (US), 2002).
42. Sheikh, S., Migliorini, D. & Lang, N. CAR T-based therapies in lymphoma: a review of current practice and perspectives. *Biomedicines* **10**, 1960 (2022).
43. Mussetti, A. & Sureda, A. Second-line CAR T cells for lymphomas. *Lancet* **399**, 2247–2249 (2022).
44. Chaudhari, K., Rizvi, S. & Syed, B. A. Non-Hodgkin lymphoma therapy landscape. *Nat. Rev. Drug Discov.* **18**, 663–664 (2019).
45. Younes, A. et al. The landscape of new drugs in lymphoma. *Nat. Rev. Clin. Oncol.* **14**, 335–346 (2017).
46. Neal, J. T. et al. Organoid modeling of the tumor immune microenvironment. *Cell* **175**, 1972–1988.e16 (2018).
47. Egle, A., Harris, A. W., Bath, M. L., O'Reilly, L. & Cory, S. VavP-Bcl2 transgenic mice develop follicular lymphoma preceded by germinal center hyperplasia. *Blood* **103**, 2276–2283 (2004).
48. Zhang, X. et al. CellMarker: a manually curated resource of cell markers in human and mouse. *Nucleic Acids Res.* **47**, D721–D728 (2019).
49. Reimold, A. M. et al. Plasma cell differentiation requires the transcription factor XBP-1. *Nature* **412**, 300–307 (2001).
50. Shi, W. et al. Transcriptional profiling of mouse B cell terminal differentiation defines a signature for antibody-secreting plasma cells. *Nat. Immunol.* **16**, 663–673 (2015).
51. Nutt, S. L. & Kee, B. L. The transcriptional regulation of B cell lineage commitment. *Immunity* **26**, 715–725 (2007).
52. Hwang, I.-Y., Park, C., Harrison, K. & Kehrl, J. H. Biased S1PR1 signaling in B cells subverts responses to homeostatic chemokines, severely disorganizing lymphoid organ architecture. *J. Immunol.* **203**, 2401–2414 (2019).
53. Hodson, D. J. et al. Regulation of normal B-cell differentiation and malignant B-cell survival by OCT2. *Proc. Natl Acad. Sci. USA* **113**, E2039–46 (2016).
54. Chu, T., Wang, Z., Pe'er, D. & Danko, C. G. Cell type and gene expression deconvolution with BayesPrism enables Bayesian integrative analysis across bulk and single-cell RNA sequencing in oncology. *Nat. Cancer* **3**, 505–517 (2022).
55. Kleshchevnikov, V. et al. Cell2location maps fine-grained cell types in spatial transcriptomics. *Nat. Biotechnol.* **40**, 661–671 (2022).
56. Battistello, E. et al. Pan-SRC kinase inhibition blocks B-cell receptor oncogenic signaling in non-Hodgkin lymphoma. *Blood* **131**, 2345–2356 (2018).
57. Noy, A. et al. Durable ibrutinib responses in relapsed/refractory marginal zone lymphoma: long-term follow-up and biomarker analysis. *Blood Adv.* **4**, 5773–5784 (2020).
58. Laursen, M. B. et al. Human B-cell cancer cell lines as a preclinical model for studies of drug effect in diffuse large B-cell lymphoma and multiple myeloma. *Exp. Hematol.* **42**, 927–938 (2014).
59. Chapuy, B. et al. Diffuse large B-cell lymphoma patient-derived xenograft models capture the molecular and biological heterogeneity of the disease. *Blood* **127**, 2203–2213 (2016).
60. Zhang, L. et al. B-cell lymphoma patient-derived xenograft models enable drug discovery and are a platform for personalized therapy. *Clin. Cancer Res.* **23**, 4212–4223 (2017).
61. Wagar, L. E. et al. Modeling human adaptive immune responses with tonsil organoids. *Nat. Med.* **27**, 125–135 (2021).
62. Bankhead, P. et al. QuPath: open source software for digital pathology image analysis. *Sci. Rep.* **7**, 16878 (2017).
63. Greenwald, N. F. et al. Whole-cell segmentation of tissue images with human-level performance using large-scale data annotation and deep learning. *Nat. Biotechnol.* **40**, 555–565 (2022).
64. Schapiro, D. et al. MCMICRO: a scalable, modular image-processing pipeline for multiplexed tissue imaging. *Nat. Methods* **19**, 311–315 (2022).
65. R Core Team. R: A Language and Environment for Statistical Computing (2023).

Acknowledgements

We would like to express our sincere gratitude to all the patients who generously participated in this study for their invaluable contribution. We also thank the histology, bioimaging, and optics platform, the flow cytometry, and the gene expression facilities at EPFL for their technical support, Dr. John Huang for his excellent technical support with the hydrogel and for providing the rheology data, Dr. Olaia Naveiras for the infrastructure, and Dr. Gonzalez and Dr. Perentes for their participation in the collection of surgical biopsies. This work has been supported by the Accentus Foundation (to A.S.M. and E.O.), the Fondazione San Salvatore (to A.S.M. and E.O.), the Fondation Aclon and PHRT (grant number 2021/553) (to E.O.), and the ISREC foundation TANDEM program (to A.C. and E.O.). J.E. is supported by the SAMS national MD-PhD grant sponsored by the Krebsforschung Schweiz (SAMS grant n° 12/22). D.T. is supported by the Personalized Health and Related Technologies (PHRT) iPostdoc Project (grant no. 2022-476).

Author contributions

A.S.M. methods development, experimental studies, analysis; J.E. acquisition of clinical samples and data; D.S., D.T., and M.V. computational analyses; D.M. and I.L. pathology assessment; A.C. patient recruitment; T.K., R.D., and A.C. accessibility of human samples; G.C.

supervision of the computational analyses; A.S.M. and E.O. designed and supervised the study; E.O., A.S.M., J.E., and D.S. wrote the manuscript with input from all the authors.

Competing interests

The authors declare no competing interests.

Additional information

Supplementary information The online version contains supplementary material available at https://doi.org/10.1038/s41467-024-55098-w.

Correspondence and requests for materials should be addressed to Albert Santamaria-Martínez or Elisa Oricchio.

Peer review information *Nature Communications* thanks the anonymous reviewers for their contribution to the peer review of this work. A peer review file is available.

Reprints and permissions information is available at http://www.nature.com/reprints